INORGANIC CHEMISTRY FRONTIERS

RESEARCH ARTICLE

View Article Online
View Journal

Cite this: DOI: 10.1039/d6qi00251j

In situ dual-site passivation of all-inorganic perovskite quantum dots using zwitterionic taurine for enhanced defect resistance

Jun Ho Choi, †[a] Jin Young Kim, †[b] Yu Min Lee, [b] Huiseong Lee, [a] Jeong Wan Park [b] and Dong Hwan Wang *[a,b]

Metal halide perovskite quantum dots (PQDs) possess exceptional optical properties but suffer from structural instability under thermal, moisture, and light exposure due to the dynamic bonding of long-chain organic ligands and the ionic nature of their crystal structure. These instabilities increase surface defects and non-radiative recombination, limiting their potential for next-generation optoelectronic devices. In this work, we present a strategy to simultaneously control surface passivation by introducing the zwitterionic ligand taurine during the *in situ* synthesis of $CsPbBr_3$ PQDs. The SO_3^- group of taurine strongly coordinates with surface Pb^{2+}, while the NH_3^+ group electrostatically interacts with Br^- ions, enabling effective dual-site passivation at the PQD surface. As a result, taurine-based PQDs exhibit enhanced QY compared with PQDs synthesized using conventional long-chain ligands. The PQDs also maintain strong photoluminescence in aqueous environments for 140 h and demonstrate improved thermal stability at 120 °C relative to pristine $CsPbBr_3$ PQDs. Furthermore, dual-site passivation lowers trap density, while the short taurine ligand enhances charge mobility, yielding electronic properties favorable for device applications. This study demonstrates that zwitterionic ligand engineering is an effective strategy to simultaneously improve the stability and performance of perovskite quantum dots, offering a promising pathway for the development of high-performance optoelectronic devices.

Received 3rd February 2026,
Accepted 30th April 2026

DOI: 10.1039/d6qi00251j

rsc.li/frontiers-inorganic

1. Introduction

Metal halide perovskite quantum dots (PQDs) have attracted considerable attention as promising materials for next-generation light-emitting, sensing, and optoelectronic devices due to their narrow full width at half maximum (FWHM), high photoluminescence quantum yield (QY), and composition-dependent bandgap tunability.[1–7] Their precisely adjustable emission wavelengths, facilitated by halide composition control and quantum confinement effects, combined with low-temperature, solution-processable synthesis, offer substantial advantages over conventional CdSe and InP quantum dots. Inorganic $CsPbX_3$ (X = Cl, Br, I) PQDs, in particular, exhibit strong potential in applications such as QLEDs, photodetectors, lasers, and solar energy harvesting.[8–15] These advantages stem from their defect tolerance, relatively high structural stability compared with CdSe and InP QDs, excellent color purity, and high luminous efficiency.

Despite these benefits, the practical implementation of $CsPbX_3$ PQDs is fundamentally limited by their structural instability. This instability arises from the dynamic binding property of long-chain organic surface ligands and the inherently ionic nature of the perovskite crystal structure.[16–23] Long-chain ligands are essential during nucleation and growth, but they readily desorb even at room temperature, and ligand loss accelerates under thermal stress, illumination, moisture, or polar environments. Ligand desorption increases cationic and anionic surface defect densities, promoting nonradiative recombination and causing rapid degradation of structural and photoelectrical properties. Consequently, developing more strongly binding and robust surface ligands has emerged as a critical strategy for stabilizing PQDs. Among the various approaches, zwitterionic ligand engineering, leveraging ligands that bear both positively and negatively charged functional groups, has shown notable promise for enhancing ligand binding strength, suppressing defect sites, and improving long-term luminescence stability.[24–31]

Recent studies have demonstrated that ionic or multifunctional ligands containing multidentate or strongly coordinat-

[a]School of Integrative Engineering, Chung-Ang University, 84 Heukseok-ro, Dongjak-gu, Seoul 06974, Republic of Korea. E-mail: king0401@cau.ac.kr
[b]Department of Intelligent Semiconductor Engineering, Chung-Ang University, 84 Heukseok-ro, Dongjak-gu, Seoul 06974, Republic of Korea
† These authors contributed equally to this work.

ing functional groups can effectively passivate surface defects in perovskite quantum dots (PQDs). Such ligands, incorporating functionalities such as anionic moieties (*e.g.*, $-SO_3^-$, $-COO^-$) and cationic groups (*e.g.*, $-NH_3^+$), have been explored to mitigate cationic and/or anionic surface defects.[32–38] For example, Yang *et al.* reported that strong SO_3^-–Pb^{2+} coordination improved ligand retention and maintained PL during purification.[39] while Wang *et al.* observed reduced defect density and enhanced LED efficiency through surface reconstruction effects induced by ionic functional groups.[40] More recently, true zwitterionic ligands, which intrinsically contain both positive and negative charges within a single molecular framework (*e.g.*, $-NH_3^+/-SO_3^-$ or $-NH_3^+/-COO^-$), have been highlighted for their potential to simultaneously interact with both cationic and anionic surface sites, thereby improving long-term stability and device performance.[41] However, most reported strategies rely on long-chain alkyl zwitterionic ligand and post-synthetic ligand exchange or purification-mediated treatments, which remain limited by the inherently long ligand chains commonly used, an issue that adversely affects charge transport.

In this work, we introduce a strategy for incorporating the zwitterionic ligand taurine directly during the *in situ* synthesis of $CsPbBr_3$ PQDs. The SO_3^- group of taurine strongly coordinates with surface Pb^{2+} ions, while the NH_3^+ group electrostatically interacts with bromide ions, enabling simultaneous suppression of cationic and anionic defects. As a result, taurine–$CsPbBr_3$ PQDs exhibit improved colloidal dispersion, enhanced PL efficiency, and markedly increased stability against air, water, and thermal stress compared with PQDs synthesized using conventional long-chain organic ligands. Additionally, the intrinsically short chain length of taurine reduces trap density and improves charge mobility, offering significant performance advantages for PQDs-based optoelectronic devices.[39,42–48] Overall, this work presents an effective surface-engineering strategy for $CsPbBr_3$ PQDs using zwitterionic ligands and demonstrates the strong potential of zwitterionic functional group incorporation for enabling stable, high-performance perovskite-based optoelectronic devices.

2. Experimental

2.1. Chemical materials

Cesium bromide (CsBr, 99.99%, TCI), lead bromide ($PbBr_2$, 99.99%, TCI), taurine (99%, Sigma-Aldrich), *n*-octylamine (99%, Sigma-Aldrich), oleic acid (90%, Sigma-Aldrich), *N*,*N*-dimethylformamide (DMF, ≥99.9%, Sigma-Aldrich), toluene (99.8%, Sigma-Aldrich), *n*-hexane (95%, Sigma-Aldrich), [6,6]-phenyl-C_{61}-butyric acid methyl ester ($PC_{60}BM$, >99.5%, 1-material), SnO_2 (15% in H_2O colloidal dispersion solution, Alfa Aesar) and rhodamine B (analytical standard, Sigma-Aldrich) were used for QY measurement. Deionized water (DIW) was purified using a Water Purification System (Human, POWER), producing water with a resistivity of 18.2 MΩ cm.

2.2. Synthesis of pristine $CsPbBr_3$ PQD solution

CsBr (0.0213 g, 0.01 mmol) and $PbBr_2$ (0.036 g, 0.01 mmol) were added to a flask along with 1 mL of DMF and 15 μL of octylamine. The mixture was sonicated for 2 min to obtain a clear precursor solution. In a separate 10 mL flask, 5 mL of toluene and 1 mL of oleic acid were combined and stirred at 600 rpm. The precursor solution was rapidly injected into this toluene/oleic acid mixture, immediately yielding a yellow–green dispersion. After 5 s, the solution was centrifuged at 8000 rpm for 5 min. The supernatant was discarded, and the precipitate was dried for 2 min. The dried solid was redispersed in 2 mL of hexane and centrifuged again, and the supernatant was collected to yield a hexane dispersion of $CsPbBr_3$ PQDs.

2.3. Synthesis of taurine–$CsPbBr_3$ PQDs solution

Taurine solutions of various concentrations (0, 6, 12, and 24 wt%) were prepared by dissolving taurine in 1 mL of DMF in a three-neck flask. The mixture was heated to 60 °C under a N_2 atmosphere and stirred for 30 min to ensure the zwitterionic property of taurine in DMF solution. The perovskite precursors CsBr (0.0213 g, 0.01 mmol) and $PbBr_2$ (0.036 g, 0.01 mmol) were placed in a separate 10 mL flask, and 1 mL of DMF along with the prepared taurine solution were added. This mixture was sonicated for 3 min to promote coordination between the sulfonate group and Pb^{2+}. Subsequently, 15 μL of octylamine was added and the solution was sonicated for an additional 2 min. In a separate 10 mL flask, 5 mL of toluene and 1.7 mL of oleic acid were stirred at 600 rpm. The taurine-containing precursor solution was then rapidly injected into this mixture, immediately forming a yellow–green solution. After 5 s, the solution was centrifuged at 8000 rpm for 5 min. The supernatant was discarded and the precipitate was dried and the solid was redispersed in 2 mL of hexane. After re-dispersion, the supernatant was collected to obtain taurine–$CsPbBr_3$ PQDs dispersed in hexane.

2.4. Device fabrication

Glass/ITO substrates were cleaned by sequential ultrasonication in DIW, acetone, and isopropanol for 20 min each, followed by N_2 drying and UV–ozone treatment for 20 min. SnO_2 was then spin-coated onto the ITO substrate at 3000 rpm for 30 s and annealing for 30 min at 150 °C. $CsPbBr_3$ and taurine–$CsPbBr_3$ PQDs were spin-coated at 1000 rpm for 10 min inside a glovebox (Ar atmosphere). A 1 : 1 (v/v) mixture of chloroform and chlorobenzene (0.5 mL total) containing $PC_{60}BM$ at 200 g L^{-1} was then spin-coated at 2000 rpm for 40 s. Finally, a 100 nm Ag electrode was deposited by thermal evaporation.

2.5. Characterization

The $CsPbBr_3$ and taurine–$CsPbBr_3$ PQDs were characterized using transmission electron microscopy (TEM) with a JEOL JEM-2100 instrument and scanning transmission electron microscopy (STEM) with a JEOL JEM-ARM200F. The X-ray diffr-

action (XRD) patterns of the perovskite powders were obtained using a Bruker AXS New D8-Advance diffractometer equipped with Cu–Kα radiation. Film thickness and cross-sectional morphology were examined using a SIGMA field-emission scanning electron microscope (FE-SEM, Carl Zeiss) operated at an accelerating voltage of 5 kV. Functional groups of the PQDs were analyzed using a Nicolet 6700 Fourier transform infrared (FTIR) spectrometer in attenuated total reflection (ATR) mode. Absorbance measurements of the $CsPbBr_3$ and taurine–$CsPbBr_3$ PQDs dispersed in *n*-hexane were recorded using a Perkin–Elmer Lambda 365 spectrophotometer. Photoluminescence (PL) spectra were collected using a Hitachi F-7000 fluorescence spectrophotometer with a monochromatic Xe lamp as the excitation source. Relative QY values for $CsPbBr_3$ and taurine–$CsPbBr_3$ PQDs were determined using the Hitachi F-7000 and the Perkin–Elmer Lambda 365 spectrophotometers, with rhodamine B as the reference dye. The absorbance of the reference solution was adjusted to approximately 0.1 prior to measurement. The stability of the $CsPbBr_3$ and taurine–$CsPbBr_3$ PQDs was assessed under various conditions through storage tests conducted under an ambient atmosphere. X-ray photoelectron spectroscopy (XPS) analysis of PQDs thin films was performed using a K-alpha instrument (Thermo Fisher Scientific).

3. Results and discussion

As schematically illustrated in Fig. 1, $CsPbBr_3$ PQDs and taurine–$CsPbBr_3$ PQDs were synthesized using a slightly modified split-ligand-mediated reprecipitation method.[49] In this system, the sulfonate group of taurine forms a direct strong coordination bond with the surface Pb^{2+} ions of the PQDs. The wt% of taurine was defined relative to the $PbBr_2$ content. Taurine was introduced *in situ* into the perovskite precursor solution to promote efficient anchoring of the sulfonate groups to the PQDs surface. In the conventional synthesis route, taurine does not fully dissolve when mixed with the DMF/octylamine-based perovskite precursor under ultrasonication. To address this solubility limitation, DMF and taurine were first added to a three-necked flask and stirred at 60 °C for 30 min under a nitrogen atmosphere to ensure complete dissolution. The resulting taurine–DMF solution was then added to the perovskite precursor, followed by the addition of octylamine, and the mixture was ultrasonicated to allow full incorporation of taurine. Upon injecting the precursor solution into a nonpolar solvent, $CsPbBr_3$ PQDs were formed due to the solubility contrast, while sulfonate groups simultaneously coordinated to surface Pb^{2+} sites. The proposed surface passivation mechanism of taurine on $CsPbBr_3$ PQDs is schematically shown in Fig. 1. Typically, $CsPbBr_3$ PQDs synthesized at room temperature are capped with long-chain organic ligands such as oleic acid and oleylamine, which bind dynamically to the PQD surface. Although this dynamic binding initially stabilizes the PQDs surface, ligand desorption readily occurs over time, during purification, or under polar, moist, or thermal environments. As a result, the formation of Br vacancies and undercoordinated Pb^{2+} sites increases non-radiative recombination pathways, thereby degrading optical efficiency and structural stability.[16,39,41] Taurine, a zwitterionic ligand, provides two complementary binding modes that are not accessible to conventional single-functional ligands. First, the sulfonate ($-SO_3^-$) group forms a strong Lewis acid–base interaction with exposed Pb^{2+} ions. This binding mode is known to exhibit greater coordination strength, higher stability and bond dissociation energy than carboxylate-based ligands, allowing sulfonates to more effectively suppress Pb^{2+} exposure.[39,41,48] Second, the positively charged ammonium ($-NH_3^+$) group forms electrostatic interactions with nearby bromide ions or halide vacancies, inhibiting Br loss and preventing the formation of additional halide vacancies.

This dual-site passivation reduces the density of vacancy formation and leads to a reduction in surface trap states.[45,46] Because taurine simultaneously passivates both Pb- and Br-related surface defects within a single ligand, unlike conventional long-chain organic ligands, its incorporation during $CsPbBr_3$ PQD synthesis yields higher QY, improved long-term storage stability, and enhanced resistance to water- and thermally induced degradation.

TEM imaging and particle-size distribution analysis were conducted to evaluate the effect of taurine concentration on the morphology and size of $CsPbBr_3$ PQDs. As shown in Fig. 2a–d, both pristine $CsPbBr_3$ PQDs and taurine–$CsPbBr_3$ PQDs exhibit a cubic crystal structure. The particle-size distributions reveal mean diameters of 10.75 nm for the pristine sample, 10.24 nm for 6 wt% taurine, 10.49 nm for 12 wt% taurine, and 10.78 nm for 24 wt% taurine. Taurine treatment did not have a significant effect on particle size, and taurine treatment inhibited particle aggregation. This behavior is attributed to the dynamic binding nature of long-chain ligands such as oleic acid and octylamine, which readily desorb during purification or air exposure, leading to surface instability and promoting interparticle aggregation.[16] In contrast, the taurine-incorporated samples show a tendency toward suppressed aggregation due to effective surface immo-

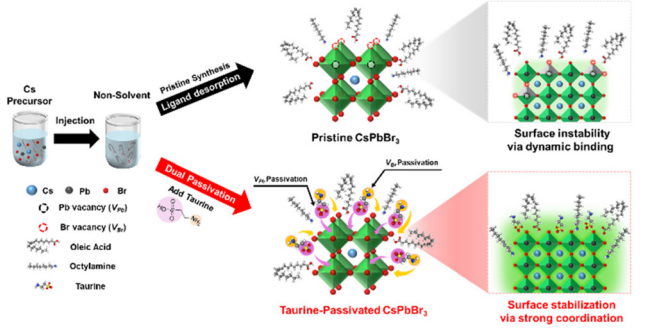

Fig. 1 Schematics of pristine $CsPbBr_3$ and zwitterionic taurine–$CsPbBr_3$ PQD synthesis method, and the surface passivation mechanism of perovskite crystals.

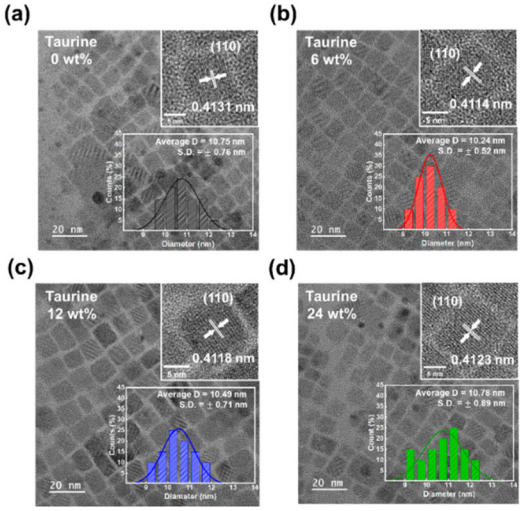

Fig. 2 TEM and HR-TEM images of $CsPbBr_3$ PQDs synthesized with different taurine loadings: (a) 0, (b) 6, (c) 12, and (d) 24 wt% and corresponding particle size distributions.

bilization, where the sulfonate ($-SO_3^-$) groups strongly coordinate to surface Pb^{2+} sites and the ammonium ($-NH_3^+$) groups electrostatically interact with surface bromide ions. This effect is most pronounced for the 6 wt% taurine sample, in which a tendency toward a narrower particle-size distribution and reduced aggregation is observed. At higher taurine loadings (12 wt% and 24 wt%), however, excess ligands partially hinder precursor diffusion and surface rearrangement, inducing ligand clustering and resulting in reduced morphological uniformity compared with the optimized 6 wt% sample.

The crystal structures of the synthesized $CsPbBr_3$ and taurine–$CsPbBr_3$ PQDs were examined using X-ray diffraction (XRD). As shown in Fig. 3a, all samples show diffraction patterns characteristic of cubic-phase $CsPbBr_3$ PQDs, indicating high crystallinity. The diffraction peaks of taurine–$CsPbBr_3$ PQDs exhibit a shift to higher 2θ values relative to the pristine sample (see Table S1). According to Bragg's law ($n\lambda = 2d \sin\theta$), the diffraction angle θ is inversely related to the interplanar spacing d. Therefore, a decrease in d leads to an increase in θ, corresponding to a shift toward higher 2θ values. The peak shifts to higher 2θ observed in the taurine-containing samples thus indicate a slight reduction in lattice spacing. This trend is qualitatively consistent with the lattice spacing variations estimated from HR-TEM analysis of the (110) plane, indicating a lattice-level modulation induced by taurine incorporation. The Fourier transform infrared (FT-IR) spectra in Fig. 3b provide further insight into the bonding and vibrational characteristics of the PQDs. All samples show vibrations associated with the hydrocarbon chains of native ligands (ν(C–H_x) and ν(C═O)) from oleic acid and octylamine. Taurine-containing samples additionally exhibit peaks assigned to ammonium (ν(N–H_3^+)) and sulfonate (ν_{as}(S═O)) vibrations, confirming incorporation of taurine's zwitterionic functional groups on the $CsPbBr_3$ PQDs surface (detailed assignments are presented in Fig. S1). Fig. 3c shows the PL intensity and absorbance of $CsPbBr_3$ PQDs with different taurine concentrations. The PL peak positions for $CsPbBr_3$ are 527.5, 517.6, 516.3, and 521.3 nm for 0, 6, 12, and 24 wt%, respectively in Table S2. The overall blue shift observed upon taurine addition results in the observed particles being located in the weak quantum confinement region, as shown in Fig. S2. As shown in Fig. S3, the bandgap values extracted from Tauc plots are provided to facilitate the interpretation of the electronic structure. As shown in Fig. S4, the PL intensity of taurine–$CsPbBr_3$ PQDs followed the trend of 6 > 12 > 24 > 0 wt%, with the 6 wt% taurine sample exhibiting the most pronounced increase compared with pristine $CsPbBr_3$ PQDs. Relative QY values were determined using rhodamine B dissolved in ethanol (QY = 0.65) as the standard.[50–52] The relationship between the standard and the sample for the comparative QY calculation is expressed by eqn (1):

$$\Phi_P = \Phi_R \cdot \frac{F_P \cdot \varepsilon_R \cdot C_R \cdot L_R \cdot {n_P}^2}{F_R \cdot \varepsilon_P \cdot C_P \cdot L_P \cdot {n_S}^2} = \Phi_R \cdot \frac{F_P \cdot A_R \cdot {n_P}^2}{F_R \cdot A_P \cdot {n_R}^2} = \Phi_R \cdot \frac{\mathrm{Grad}_P \cdot {n_P}^2}{\mathrm{Grad}_R \cdot {n_R}^2} \quad (1)$$

where F, L, and n represent the integrated PL area, optical path length, and solvent refractive index, respectively. ε, C, and Φ denote the molar absorptivity, concentration, and relative quantum yield. Because the three parameters ε, C, and Φ are linearly related to absorbance (A) through the Beer–Lambert law, the QY can be expressed in terms of the gradient obtained from the slope of PL intensity *versus* absorbance. Subscripts R and P refer to the reference (rhodamine B) and the PQD sample, respectively. The PL and absorbance spectra of rhodamine B used for relative QY calculations are provided in Fig. S5 and S6. The variables applied in the relative QY calculations are summarized in Table 1 and Table S3. As shown in Fig. 3d, the relative QY values of the taurine–$CsPbBr_3$ PQDs were 0.723,

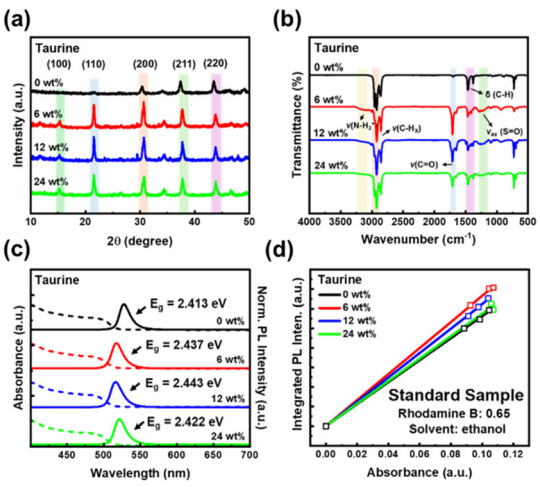

Fig. 3 (a) XRD patterns, (b) FT-IR spectra, (c) normalized UV–vis absorption and PL spectra, and (d) relative quantum yield for synthesized $CsPbBr_3$ PQDs calculated with reference to a rhodamine B standard value of 0.65.

Table 1 Parameters used to determine the relative QY of $CsPbBr_3$ PQDs

Taurine	Refractive index	Gradient (F A^{-1})	Quantum yield
0 wt%	1.375	1.13×10^5	0.723
6 wt%	1.375	1.33×10^5	0.867
12 wt%	1.375	1.25×10^5	0.811
24 wt%	1.375	1.15×10^5	0.750

0.867, 0.811, and 0.750 for 0, 6, 12, and 24 wt% taurine, respectively. We further evaluated the optimal conditions by adding the wt% taurine content condition. As shown in Fig. S7 and Table S4, among the key performance indicators of PQDs, the quantum yield (QY) was compared, and the results showed that the 6 wt% condition yielded the best QY. The QY values for each wt% condition show a decreasing trend with increasing concentration, starting from 6 wt%. Therefore, the maximum QY observed at 6 wt% is considered a reliable indicator of the most effective surface defect passivation achieved through taurine addition. The observed performance degradation at higher concentrations (12 wt% and 24 wt%) is due to ligand clustering due to excess ligand. In this case, ligands attached to the particle surface or free ligands tend to aggregate, resulting in a decrease in both luminescence performance and stability. Because the relative QY values were determined under identical absorption conditions, the observed PL intensity trends are consistent with the corresponding QY variations. This enhancement is attributed to the zwitterionic bifunctional groups of taurine, which effectively reduce perovskite surface defects and bromide vacancies, thereby significantly suppressing non-radiative recombination and greatly improving the optical performance of the PQDs.

To investigate whether the observed enhancement in PLQY originates from the suppression of non-radiative recombination processes, time-resolved photoluminescence (TRPL) measurements were conducted. The TRPL decay curves were analysed by selecting the effective decay region, excluding the initial rise immediately after photoexcitation as well as the noise-dominated tail at long delay times. t_0 avoids reliance on assumptions associated with a specific exponential decay model, and the average lifetime was defined using the first-moment mean lifetime, $\langle t \rangle$. The $\langle t \rangle$ calculation is expressed by eqn (2):[53]

$$\langle t \rangle = \frac{\int_{t_1}^{t_2} (t - t_0) I(t) \mathrm{d}t}{\int_{t_1}^{t_2} I(t) \mathrm{d}t} \quad (2)$$

$I(t)$ is the baseline-corrected PL intensity and t is the delay time. The peak position of the decay curve after baseline correction was defined as t_0. To systematically exclude the rising edge, the integration start time was set to $t_1 = t_0$ and the integration end time t_2 was fixed at 250 ns for all samples to exclude the noise-dominated tail region. The same criteria were applied to all samples to ensure reproducibility and comparability. As a result, t_0 values of 11.23, 19.53, 16.30 and 11.23 ns and average lifetimes of 38.20, 44.60, 41.92, and 38.74 ns were obtained for the samples with taurine concentrations of 0, 6, 12, and 24 wt%, respectively, with the 6 wt% taurine–$CsPbBr_3$ PQDs exhibiting the longest $\langle t \rangle$. This prolonged lifetime indicates that non-radiative recombination pathways associated with surface defects are effectively suppressed upon taurine incorporation. The dual-site binding mechanism of taurine plays a critical role in this process: the sulfonate group coordinates with undercoordinated Pb^{2+} sites, while the ammonium group compensates halide-related vacancies. Such simultaneous passivation of cationic and anionic defect sites effectively suppresses defect-induced trap states, thereby reducing trap-assisted non-radiative recombination. In contrast, the $\langle t \rangle$ values for the 12 wt% and 24 wt% samples show a decreasing trend, which can be attributed to surface saturation effects or the emergence of localized non-radiative pathways at excessive ligand concentrations. These TRPL results qualitatively agree well with the PLQY trends, both identifying 6 wt% as the optimal taurine concentration and providing evidence that taurine-based surface passivation effectively enhances the optical properties of $CsPbBr_3$ PQDs. Detailed TRPL decay curves and the corresponding analysis procedures are provided in Fig. S8.

X-ray photoelectron spectroscopy (XPS) was employed to investigate the surface chemical states and bonding environments of $CsPbBr_3$ PQDs with and without taurine incorporation. To elucidate the influence of taurine on surface interactions, the core-level spectra of Cs, Pb, Br, S, and N were individually analyzed, as shown in Fig. 4a–e. Fig. 4a shows the Cs 3d spectra.

The pristine $CsPbBr_3$ PQDs exhibit Cs $3d_{3/2}$ and Cs $3d_{5/2}$ peaks at 738.01 and 724.07 eV, respectively. After incorporating taurine at 6 wt%, both peaks shift slightly toward higher binding energies, appearing at 738.38 and 724.50 eV. This

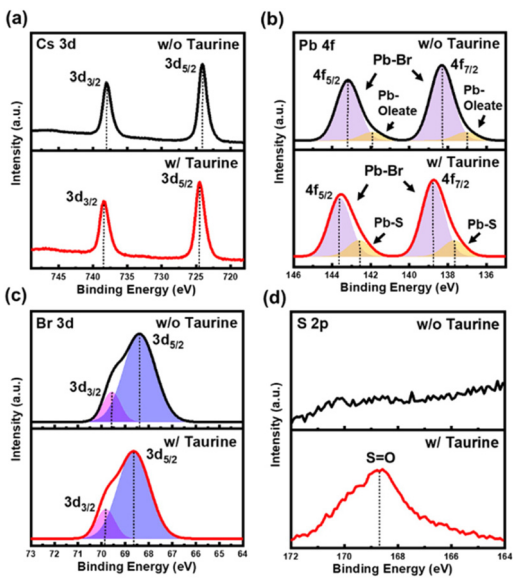

Fig. 4 XPS spectra of w/o and w/ taurine (6 wt%) $CsPbBr_3$ PQDs: (a) Cs 3d, (b) Pb 4f, (c) Br 3d, (d) S 2p.

shift is not due to direct chemical binding of Cs^+ ions to taurine, but rather to changes in the local electrostatic environment induced by surface reorganization following the introduction of taurine. More pronounced changes are observed in the Pb 4f spectra (Fig. 4b). In the pristine sample, the Pb $4f_{5/2}$ and Pb $4f_{7/2}$ peaks can be deconvoluted into two components corresponding to Pb–Br interactions (143.18 and 138.29 eV) and Pb–oleate surface species (141.93 and 137.08 eV). Upon taurine incorporation, the Pb–Br-related peaks shift to higher binding energies (143.65 and 138.78 eV), while the Pb–oleate-associated component evolves into a new feature located at 142.57 and 137.66 eV. This newly emerged component is attributed to S-related surface interactions (denoted as Pb–S), indicating a modification of the Pb-centered surface bonding environment. The Br 3d spectra (Fig. 4c) also exhibit systematic binding-energy shifts. The pristine PQDs show Br $3d_{3/2}$ and Br $3d_{5/2}$ peaks at 69.55 and 68.37 eV, respectively, whereas the taurine-treated sample shows corresponding peaks at 69.84 and 68.65 eV. These shifts suggest a modification of the Br-related surface bonding state and local electrostatic potential following taurine incorporation. Fig. 4d shows the S 2p spectra. No discernible S 2p signal is detected in the pristine sample, while a distinct S 2p peak centered at 168.70 eV emerges after taurine incorporation, which is characteristic of sulfonate (S═O) species. This observation provides direct evidence for the incorporation of taurine-derived functional groups on the PQD surface. Finally, the N 1s spectra (Fig. S9) shows a peak at 401.45 eV for the pristine sample, which shifts slightly to 401.65 eV after taurine incorporation. This binding-energy range corresponds to ammonium-like (NH_3^+) nitrogen species, indicating the presence of positively charged taurine moieties at the PQD surface. So, taurine–$CsPbBr_3$ PQDs strengthened electrostatic interaction at the PQD surface. Overall, the emergence of the S 2p signal, the evolution of Pb 4f surface components, and the consistent binding-energy shifts observed across Cs, Pb, Br, and N core levels collectively demonstrate that taurine incorporation effectively modulates the surface chemical environment and local electrostatic potential of $CsPbBr_3$ PQDs. These results support the role of taurine as an effective *in situ* surface passivation strategy rather than a conventional post-synthetic ligand-exchange process.

The inherently low stability of PQDs in air, aqueous, and thermal environments is a well-known limitation for their practical application.[54] To assess the effect of taurine on stability, we conducted contact angle, surface energy, and environmental stability measurements in aqueous, thermal, and ambient air environments. The stability measurements were conducted under ambient laboratory conditions at approximately 25 ± 2 °C and 40 ± 5% relative humidity. To evaluate the resistance to water of PQDs, we fabricated thin films of $CsPbBr_3$ and taurine–$CsPbBr_3$ PQDs, and DIW droplets were dropped to determine contact angles and surface energies. The surface energy was calculated using DIW and diiodomethane (DIM) droplets *via* the Owens–Wendt method,[55] with the relevant variables summarized in Table S5. The relationship between the contact angle and the surface energy for the samples is expressed by eqn (3) and (4):

$$\gamma_{sl} = \gamma_{sv} + \gamma_{lv} - 2\sqrt{\gamma_{sv}^{d}\gamma_{lv}^{d}} - 2\sqrt{\gamma_{sv}^{p}\gamma_{lv}^{p}} \quad (3)$$

$$\gamma_{lv}(1 + \cos\theta) = 2\sqrt{\gamma_{sv}^{d}\gamma_{lv}^{d}} + 2\sqrt{\gamma_{sv}^{p}\gamma_{lv}^{p}} \quad (4)$$

where θ is the contact angle between the droplet and the thin film coated with taurine–$CsPbBr_3$ PQDs, and γ_{lv}, γ_{lv}^{d}, and γ_{lv}^{p} are the surface free energy and dispersive and polar components of the surface energy of the liquid droplet (DIW or DIM), respectively (eqn (3) and (4)). As shown in Fig. 5a, the contact angle increased in the order 6 wt% > 12 wt% > 24 wt% > pristine $CsPbBr_3$ PQDs, with the highest value of 65.35° observed for the 6 wt% taurine sample and the lowest value of 58.33° for the pristine $CsPbBr_3$ PQDs. Correspondingly, surface energies were lowest for the 6 wt% sample (50.79 mJ m^{-2}) and highest for pristine $CsPbBr_3$ PQDs (55.07 mJ m^{-2}). These trends can be attributed to the weak dynamic binding of long-chain organic ligands in pristine PQDs, which leads to ligand desorption and exposure of uncoordinated surface ions. The resulting surface defects reduce contact angles and increase surface energies when exposed to DIW. In contrast, the incorporation of taurine at the optimal concentration (6 wt%) enhances surface stabilization through strong dual-site passivation, improving surface immobilization and dispersion stability. This effect is reflected in the higher contact angle and lower surface energy for the 6 wt% sample. Collectively, these results indicate that taurine incorporation not only enhances water resistance but also contributes to improved long-term storage stability and thermal durability of $CsPbBr_3$ PQDs.

As shown in Fig. 5b, DIW and hexane-dispersed PQDs were mixed in a 1 : 1 ratio, forming a DIW bottom layer and a hexane-dispersed PQD top layer. Because the PQDs in hexane are in direct contact with DIW at the interface, this configur-

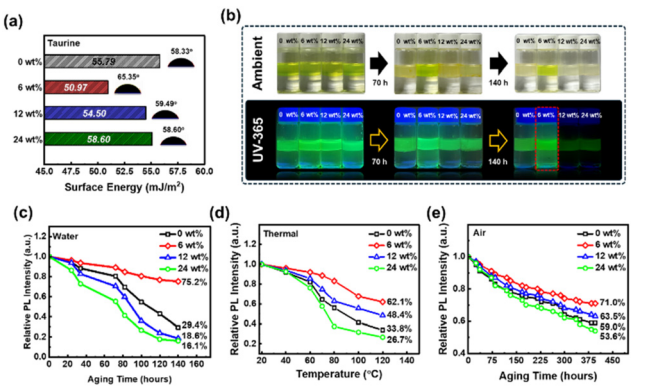

Fig. 5 (a) Surface energy and contact angle of $CsPbBr_3$ PQDs film with different amounts of taurine (0, 6, 12, and 24 wt%) measured using DIW. (b) Photograph of deionized water (DIW) and different amounts of taurine (0, 6, 12 and 24 wt%) after 0, 70 and 140 h. Relative PL intensity of $CsPbBr_3$ PQDs with different taurine contents under (c) aqueous, (d) thermal, and (e) ambient air conditions.

ation is well suited for evaluating the structural stability of the perovskite quantum dots. As shown in Fig. 5b and c, the PL intensities of all samples decreased significantly over time, except for the 6 wt% taurine sample. After 140 h, PL retention was 75.2% for the 6 wt% taurine sample, compared with 29.4% for pristine PQDs, 18.6% for 12 wt% taurine, and 16.1% for 24 wt% taurine. While the 12 wt% and 24 wt% taurine samples exhibited weak photoluminescence, and pristine $CsPbBr_3$ PQDs showed diminished emission, the 6 wt% taurine sample retained strong luminescence even after 140 h in an aqueous environment. These results indicate that strong surface passivation *via* ligand binding enhances luminescence in aqueous environments, whereas excessive ligand loading or weak ligand binding accelerates the degradation of PQD particles. Thermal stability was assessed by heating PQDs for 10 min at temperatures from 20 °C to 140 °C in 20 °C increments. As shown in Fig. 5d, PL retention at 120 °C was 62.1% for 6 wt% taurine, 48.4% for 12 wt% taurine, 33.8% for pristine PQDs, and 26.7% for 24 wt% taurine. These results demonstrate that dual-site passivation by taurine ligands effectively inhibits decomposition of the PQD particles due to the desoprtion of the surface ligands under thermal stress. PL stability under ambient air conditions is shown in Fig. 5e. After 450 h, the PL retention was 71.0% for 6 wt% taurine, 63.5% for 12 wt% taurine, 59.0% for pristine PQDs, and 53.6% for 24 wt% taurine. This behavior can be attributed to taurine's zwitterionic functional groups ($-SO_3^-$ and $-NH_3^+$), which enable dual-site passivation: the sulfonate group coordinates strongly with Pb^{2+}, while the ammonium group electrostatically interacts with halides, suppressing halide loss and reducing defect formation. Fig. S1 and Fig. 3b show that the strongest sulfonate and ammonium vibrational peaks were observed at 6 wt% taurine, followed by 12 wt% and 24 wt% taurine, indicating that only the optimal concentration enables efficient surface binding. At higher concentrations, excess taurine ligands remain unbound as free ligands, leading to ligand clustering or particle agglomeration, which significantly reduces stability. In DMF, taurine's functional groups are exposed when the PQD surface is not fully passivated, accelerating degradation, particularly in aqueous environments. This effect is more pronounced in an aqueous environment than under thermal or air conditions. Consequently, relative QY follows the order 6 wt% taurine > 12 wt% taurine > 24 wt% taurine > pristine PQDs, with excess ligand leading to lower stability over time. These results indicate that an optimal taurine concentration of 6 wt% provides the most effective defect passivation, suppressing perovskite structural degradation and enabling excellent stability under water, heat, and air exposure. Overall, the introduction of zwitterionic ligands at optimal concentrations significantly enhances the environmental stability of $CsPbBr_3$ PQDs. Therefore, the consistent stability trends observed across water, thermal, and air conditions directly correlate with the extent of taurine-induced defect passivation. The prolonged carrier lifetime observed in the TRPL measurements at 6 wt% taurine, together with the highest QY retention, confirms that balanced dual-site passivation effectively suppresses non-radiative recombination and environmental degradation.

Conventional long-chain organic ligands possess extended alkyl chains that act as electrical insulators, limiting charge transport in devices. In contrast, incorporating taurine ligands with short alkyl chains enhances charge transport relative to long-chain ligands. To quantify this effect, the space-charge-limited current (SCLC) method was employed to investigate charge transport and determine trap-state density. Electron-only devices with the configuration ITO/SnO_2/taurine–$CsPbBr_3$ PQDs/PCBM/Ag were fabricated, as illustrated in Fig. 6f.

As shown in Table 2 and Fig. 6a–d, the current–voltage characteristics of the devices were analyzed to determine the trap-filled limit voltages (V_{TFL}), which were 0.748 V, 0.339 V, 0.499 V, and 0.588 V for the 0, 6, 12, and 24 wt% taurine concentrations, respectively. The trap-state density (N_{trap}) was calculated from V_{TFL} using eqn (5):[56]

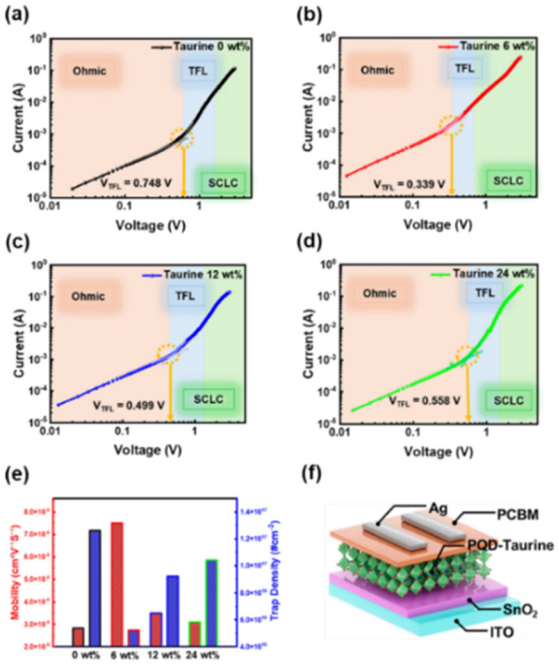

Fig. 6 *J–V* curves of electron-only SCLC devices fabricated with $CsPbBr_3$ PQDs containing different taurine concentrations: (a) 0 wt%, (b) 6 wt%, (c) 12 wt%, and (d) 24 wt%. (e) Electron mobility and trap density of taurine–$CsPbBr_3$ PQDs films extracted from SCLC measurements. (f) Schematic illustration of the electron-only device structure: ITO/SnO_2/taurine–$CsPbBr_3$ PQDs/PCBM/Ag.

Table 2 Electron-only SCLC device parameters of $CsPbBr_3$ PQDs with varying taurine contents

Taurine	V_{TFL} [V]	Electron mobility [$cm^2\ V^{-1}\ S^{-1}$]	Trap density [# cm^{-3}]
0 wt%	0.748	2.82×10^{-6}	1.26×10^{17}
6 wt%	0.339	7.50×10^{-6}	5.21×10^{16}
12 wt%	0.499	3.49×10^{-6}	9.20×10^{16}
24 wt%	0.588	3.09×10^{-6}	1.04×10^{17}

$$N_{trap} = \frac{2\varepsilon\varepsilon_0}{qd^2}V_{TFL} \quad (5)$$

In eqn (5), ε represents the permittivity of $CsPbBr_3$ PQDs, ε_0 is the permittivity of vacuum, and d is the thickness of the $CsPbBr_3$ PQDs layer, which varies with taurine wt%. The dielectric constant (ε) of $CsPbBr_3$ PQDs is 16.4. Layer thicknesses of the $CsPbBr_3$ PQDs with varying taurine concentrations were measured and found to be 44.46, 46.21, 42.43, and 42.25 nm for 0, 6, 12, and 24 wt% taurine, respectively (Fig. S10).[23,57] Charge mobility was calculated using the Mott–Gurney equation:[58]

$$J_{SCLC} = \frac{9}{8}\varepsilon_r\varepsilon\mu\frac{V^2}{d^3} \quad (6)$$

In eqn (6), μ is the electron mobility and J_{SCLC} is space-charge-limited current density. Using eqn (5) and (6), the device based on 6 wt% taurine–$CsPbBr_3$ PQDs exhibited a trap density of 5.21×10^{16} cm^{-3} and an electron mobility of 7.50×10^{-6} cm^2 V^{-1} s^{-1}, corresponding to approximately a two-fold reduction in trap density and a 2.5-fold increase in mobility compared with pristine $CsPbBr_3$ PQDs (Fig. 6e). The short-chain, zwitterionic taurine ligands effectively passivate surface defects arising from ligand desorption while mitigating the charge transport limitations associated with conventional long-chain ligands. Consequently, taurine–$CsPbBr_3$ PQDs exhibit significantly enhanced electrical and optical performance, highlighting their potential for high-performance optoelectronic applications. In addition, key performance metrics, including trap density, QY, and stability, are summarized and compared with those of previously reported $CsPbBr_3$ PQDs in Table S6, confirming the effectiveness of the present surface passivation strategy.

4. Conclusion

In this work, taurine-functionalized $CsPbBr_3$ PQDs were successfully synthesized *via* an *in situ* ligand incorporation strategy using a zwitterionic ligand. This approach effectively mitigated ligand desorption and halide loss, which are major limitations of conventional long-chain organic ligands. As a result, surface defect passivation was significantly enhanced, leading to superior optical performance, including a 1.5-fold increase in photoluminescence quantum yield compared with pristine $CsPbBr_3$ PQDs. The water and thermal stability of the PQD solutions were also markedly improved, highlighting the crucial role of dual-site coordination in maintaining structural and optical integrity under harsh conditions. Furthermore, electron-only devices fabricated with $CsPbBr_3$ PQDs at the optimal taurine concentration exhibited a 2.5-fold increase in charge mobility and a two-fold reduction in trap density relative to devices based on pristine $CsPbBr_3$ PQDs, demonstrating substantial improvements in electrical properties. Collectively, these results show that the dual-site coordination and short-chain property of taurine enable effective surface defect passivation while simultaneously enhancing device performance. This strategy provides a promising and broadly applicable approach for the development of high-stability, high-performance perovskite-based optoelectronic devices.

Author contributions

J. H. Choi and J. Y. Kim: conceptualization, methodology, formal analysis, investigation, writing – original draft, and visualization; Y. M. Lee: investigation and formal analysis; H. Lee, J. W. Park: investigation; D. H. Wang: conceptualization, methodology, writing – review & editing, supervision, project administration, and funding acquisition.

Conflicts of interest

There are no conflicts to declare.

Data availability

The data supporting this article have been included as part of the supplementary information (SI). Supplementary information is available. See DOI: **https://doi.org/10.1039/d6qi00251j**.

Acknowledgements

This research was supported by the Basic Science Research Program through the National Research Foundation of Korea (NRF), funded by the Ministry of Science and ICT (MSIT) (Grant No. 2023R1A2C2008021). This research was also supported by the Chung-Ang University Graduate Research Scholarship in 2025.

References

1 L. Protesescu, S. Yakunin, M. I. Bodnarchuk, F. Krieg, R. Caputo, C. H. Hendon, R. X. Yang, A. Walsh and M. V. Kovalenko, Nanocrystals of cesium lead halide perovskites ($CsPbX_3$, X = Cl, Br, and I): Novel optoelectronic materials showing bright emission with wide color gamut, *Nano Lett.*, 2015, **15**, 3692–3696.
2 J. Shamsi, A. S. Urban, M. Imran, L. De Trizio and L. Manna, Metal halide perovskite nanocrystals: Synthesis, post-synthesis modifications, and their optical properties, *Chem. Rev.*, 2019, **119**, 3296–3348.
3 A. Dey, J. Z. Ye, A. De, E. Debroye, S. K. Ha, E. Bladt, A. S. Kshirsagar, Z. Y. Wang, J. Yin, Y. Wang, L. N. Quan, F. Yan, M. Y. Gao, X. M. Li, J. Shamsi, T. Debnath, M. H. Cao, M. A. Scheel, S. Kumar, J. A. Steele, M. Gerhard, L. Chouhan, K. Xu, X. G. Wu, Y. X. Li, Y. N. Zhang, A. Dutta, C. Han, I. Vincon, A. L. Rogach, A. Nag, A. Samanta, B. A. Korgel, C. J. Shih, D. R. Gamelin,

D. H. Son, H. B. Zeng, H. Z. Zhong, H. D. Sun, H. V. Demir, I. G. Scheblykin, I. Mora-Seró, J. K. Stolarczyk, J. Z. Zhang, J. Feldmann, J. Hofkens, J. M. Luther, J. Pérez-Prieto, L. Li, L. Manna, M. Bodnarchuk, M. Kovalenko, M. B. J. Roeffaers, N. Pradhan, O. F. Mohammed, O. M. Bakr, P. D. Yang, P. Müller-Buschbaum, P. Kamat, Q. L. Bao, Q. Zhang, R. Krahne, R. E. Galian, S. D. Stranks, S. Bals, V. Biju, W. A. Tisdale, Y. Yan, R. L. Z. Hoye and L. Polavarapu, State of the art and prospects for halide perovskite nanocrystals, *ACS Nano*, 2021, **15**, 10775–10981.

4 S. Liang, M. Y. Zhang, G. M. Biesold, W. Choi, Y. J. He, Z. L. Li, D. F. Shen and Z. Q. Lin, Recent advances in synthesis, properties, and applications of metal halide perovskite nanocrystals/polymer nanocomposites, *Adv. Mater.*, 2021, **33**, 2005888.

5 K. Vighnesh, S. X. Wang, H. C. Liu and A. L. Rogach, Hot-injection synthesis protocol for green-emitting cesium lead bromide perovskite nanocrystals, *ACS Nano*, 2022, **16**, 19618–19625.

6 J. Y. Kim, W. Jang, T. Y. Im and D. H. Wang, Homogeneous surface attachment of functional ligands for compatible perovskite nanoparticle crystallization, *J. Alloys Compd.*, 2025, **1010**, 177990.

7 J. Y. Kim, W. Jang, J. Lim and D. H. Wang, One-pot synthesis of all-inorganic $CsPbClBr_2$ blue perovskite quantum dots via stoichiometric precursor, *Inorg. Chem.*, 2023, **62**, 11665–11673.

8 Q. S. Shan, Y. H. Dong, H. Y. Xiang, D. N. Yan, T. J. Hu, B. C. Yuan, H. Zhu, Y. F. Wang and H. B. Zeng, Perovskite quantum dots for the next-generation displays: Progress and prospect, *Adv. Funct. Mater.*, 2024, **34**, 2401284.

9 B. D. Zhao, B. B. Guo, S. Y. Xing, Z. Liu, Y. C. Yuan, Z. X. Ren, W. D. Tang, Y. X. Lian, G. Zhang, C. Zou and D. W. Di, Highly stable perovskite light-emitting diodes, *Matterials*, 2024, **7**, 772–793.

10 W. Q. Yang, S. H. Jo and T. W. Lee, Perovskite colloidal nanocrystal solar cells: current advances, challenges, and future perspectives, *Adv. Mater.*, 2024, **36**, 2401788.

11 J. Kim, J. Roh, M. Park and C. Lee, Recent advances and challenges of colloidal quantum dot light-emitting diodes for display applications, *Adv. Mater.*, 2024, **36**, 221220.

12 C. Y. Huang, C. Zou, C. Y. Mao, K. L. Corp, Y. C. Yao, Y. J. Lee, C. W. Schlenker, A. K. Y. Jen and L. Y. Lin, $CsPbBr_3$ perovskite quantum dot vertical cavity lasers with low threshold and high stability, *ACS Photonics*, 2017, **4**, 2281–2289.

13 F. Mathies, E. J. W. List-Kratochvil and E. L. Unger, Advances in inkjet-printed metal halide perovskite photovoltaic and optoelectronic devices, *Energy Technol.*, 2020, **8**, 1900991.

14 Z. Y. Yu, T. Fang and W. H. Cao, Flexible and wearable devices based on colloidal quantum dots, *Adv. Mater. Technol.*, 2025, **10**, 2401983.

15 J. Y. Kim, B. G. Kim, W. Jang and D. H. Wang, In situ interfacial-assembly perovskite quantum dot via Marangoni and capillary convection manipulation for robust luminescence, *ACS Appl. Mater. Interfaces*, 2023, **15**, 49911–49919.

16 J. De Roo, M. Ibáñez, P. Geiregat, G. Nedelcu, W. Walravens, J. Maes, J. C. Martins, I. Van Driessche, M. V. Koyalenko and Z. Hens, Highly dynamic ligand binding and light absorption coefficient of cesium lead bromide perovskite nanocrystals, *ACS Nano*, 2016, **10**, 2071–2081.

17 K. Hills-Kimball, H. J. Yang, T. Cai, J. Y. Wang and O. Chen, Recent advances in ligand design and engineering in lead halide perovskite nanocrystals, *Adv. Sci.*, 2021, **8**, 2100214.

18 Q. Y. Pan, Q. Zhao, P. X. Wei and G. R. Li, Surface ligands for perovskite quantum dots, *ChemSusChem*, 2025, **18**, e202401875.

19 L. De Trizio, I. Infante and L. Manna, Surface chemistry of lead halide perovskite colloidal nanocrystals, *Acc. Chem. Res.*, 2023, **56**, 1815–1825.

20 Y. Bai, M. M. Hao, S. S. Ding, P. Chen and L. Z. Wang, Surface chemistry engineering of perovskite quantum dots: Strategies, applications, and perspectives, *Adv. Mater.*, 2022, **34**, 2105958.

21 J. Z. Ye, M. M. Byranvand, C. O. Martnez, R. L. Z. Hoye, M. Saliba and L. Polavarapu, Defect passivation in lead-halide perovskite nanocrystals and thin films: Toward efficient LEDs and solar cells, *Angew. Chem., Int. Ed.*, 2021, **60**, 21636–21660.

22 J. Y. Kim, B. G. Kim, M. Kim, W. Jang and D. H. Wang, One-step formation of core/shell structure based on hydrophobic silane ligands for enhanced luminescent perovskite quantum dots, *J. Alloys Compd.*, 2021, **886**, 161347.

23 J. Y. Kim, J. Lim, W. Jang and D. H. Wang, Silane network passivation through lead–sulfur interaction of X-type thiol-group ligands for polar-resistance and improved mobility in perovskite quantum dots, *Adv. Opt. Mater.*, 2025, **13**, 2403039.

24 S. C. Hou, Y. Z. Guo, Y. G. Tang and Q. M. Quan, Synthesis and stabilization of colloidal perovskite nanocrystals by multidentate polymer micelles, *ACS Appl. Mater. Interfaces*, 2017, **9**, 18417–18422.

25 S. H. Xiao, X. Y. Mei and X. L. Zhang, Surface matrix regulation of perovskite quantum dots for efficient solar cells, *Energy Environ. Sci.*, 2024, **17**, 5756–5794.

26 M. Green, The nature of quantum dot capping ligands, *J. Mater. Chem.*, 2010, **20**, 5797–5809.

27 D. Choi, H. Kim, Y. Bae, S. Lim and T. Park, Perovskite colloidal quantum dots with tailored properties: Synthesis strategies and photovoltaic applications, *ACS Energy Lett.*, 2024, **9**, 2633–2658.

28 N. Fiuza-Maneiro, K. Sun, I. López-Fernández, S. Gómez-Graña, P. Müller-Buschbaum and L. Polavarapu, Ligand chemistry of inorganic lead halide perovskite nanocrystals, *ACS Energy Lett.*, 2023, **8**, 1152–1191.

29 X. Y. Zhang, Z. W. Yao, M. Deng, R. F. Wu, J. Wang, Y. Ren, C. B. Wang, G. H. Jia, L. Qian and C. Y. Xiang, Designing efficient ligand exchange strategies for the synthesis of stable perovskite nanocrystals, *J. Mater. Chem. C*, 2025, **13**, 3523–3529.

30 M. Imran, P. Ijaz, L. Goldoni, D. Maggioni, U. Petralanda, M. Prato, G. Almeida, I. Infante and L. Manna, Simultaneous cationic and anionic ligand exchange for colloidally stable $CsPbBr_3$ nanocrystals, *ACS Energy Lett.*, 2019, **4**, 819–824.

31 D. L. Jia, J. X. Chen, J. M. Qiu, H. L. Ma, M. Yu, J. H. Liu and X. L. Zhang, Tailoring solvent-mediated ligand exchange for $CsPbI_3$ perovskite quantum dot solar cells with efficiency exceeding 16.5%, *Joule*, 2022, **6**, 1632–1653.

32 D. D. Yang, X. M. Li, Y. Wu, C. T. Wei, Z. Y. Qin, C. F. Zhang, Z. G. Sun, Y. L. Li, Y. Wang and H. B. Zeng, Surface halogen compensation for robust performance enhancements of $CsPbX_3$ perovskite quantum dots, *Adv. Opt. Mater.*, 2019, **7**, 1900276.

33 Y. M. Li, M. Deng, X. Y. Zhang, L. Qian and C. Y. Xiang, Proton-prompted ligand exchange to achieve high-efficiency $CsPbI_3$ quantum dot light-emitting diodes, *Nano-Micro Lett.*, 2024, **16**, 105.

34 F. Krieg, S. T. Ochsenbein, S. Yakunin, S. ten Brinck, P. Aellen, A. Suess, B. Clerc, D. Guggisberg, O. Nazarenko, Y. Shynkarenko, S. Kumar, C. J. Shih, I. Infante and M. V. Kovalenko, Colloidal $CsPbX_3$ (X = CI, Br, I) nanocrystals 2.0: Zwitterionic capping ligands for improved durability and stability, *ACS Energy Lett.*, 2018, **3**, 641–646.

35 R. Grisorio, F. Fasulo, A. B. Muñoz-García, M. Pavone, D. Conelli, E. Fanizza, M. Striccoli, I. Allegretta, R. Terzano, N. Margiotta, P. Vivo and G. P. Suranna, In situ formation of zwitterionic ligands: changing the passivation paradigms of $CsPbBr_3$ nanocrystals, *Nano Lett.*, 2022, **22**, 4437–4444.

36 S. S. Wang, L. Du, Z. C. Jin, Y. Xin and H. Mattoussi, Enhanced stabilization and easy phase transfer of $CsPbBr_3$ perovskite quantum dots promoted by high-affinity polyzwitterionic ligands, *J. Am. Chem. Soc.*, 2020, **142**, 12669–12680.

37 H. Zhu, M. Kick, M. Ginterseder, C. J. Krajewska, T. Sverko, R. P. Li, Y. L. Lu, M. C. Shih, T. Van Voorhis and M. G. Bawendi, Synthesis of zwitterionic $CsPbBr_3$ nanocrystals with controlled anisotropy using surface-selective ligand pairs, *Adv. Mater.*, 2023, **35**, 2304069.

38 J. H. Kim, Y. R. Kim, B. Park, S. Hong, I. W. Hwang, J. Kim, S. Kwon, G. Kim, H. Kim and K. Lee, Simultaneously passivating cation and anion defects in metal halide perovskite solar cells using a zwitterionic amino acid additive, *Small*, 2021, **17**, 2005608.

39 D. D. Yang, X. M. Li, W. H. Zhou, S. L. Zhang, C. F. Meng, Y. Wu, Y. Wang and H. B. Zeng, $CsPbBr_3$ quantum dots 2.0: Benzenesulfonic acid equivalent ligand awakens complete purification, *Adv. Mater.*, 2019, **31**, 1900767.

40 J. X. Wang, Z. X. Yang, Y. Chen, H. Zhang, Y. Chen, Y. T. Bai, X. D. Jiang, B. F. Liu, J. J. Hong, Z. Z. Fang, J. Z. Gao, Z. Y. Zhou, R. S. Yu, X. Y. Song, Z. Y. Yuan, T. L. Guo, F. S. Li, Y. Y. Chen and Z. Z. Weng, Sulfonic acid ligands promote surface reconstruction of perovskite quantum dots for high-performance light-emitting diodes, *Adv. Opt. Mater.*, 2025, **13**, 2402764.

41 Z. W. Zeng, Y. H. Meng, Z. X. Yang, Y. L. Ye, Q. X. Lin, Z. Y. Meng, H. Y. Hong, S. W. Ye, Z. M. Cheng, Q. T. Lan, J. X. Wang, Y. Chen, H. Zhang, Y. T. Bai, X. D. Jiang, B. F. Liu, J. J. Hong, T. L. Guo, F. S. Li, Y. Y. Chen and Z. Z. Weng, Efficient $CsPbBr_3$ perovskite light-emitting diodes via novel multi-step ligand exchange strategy based on zwitterionic molecules, *ACS Appl. Mater. Interfaces*, 2024, **16**, 10389–10397.

42 X. Hou, Z. J. Yuan, J. L. Liu, H. Z. Ma and F. C. Yu, Taurine as a powerful passivator of perovskite layer for efficient and stable perovskite solar cells, *RSC Adv.*, 2023, **13**, 16872–16879.

43 S. H. Huang, S. H. Yang, W. C. Tsai and H. C. Hsu, Enhancing optical and thermal stability of blue-emitting perovskite nanocrystals through surface passivation with sulfonate or sulfonic acid ligands, *Nanomaterials*, 2024, **14**, 1049.

44 Y. M. Li, M. Deng, X. Y. Zhang, T. Xu, X. M. Wang, Z. W. Yao, Q. Q. Wang, L. Qian and C. Y. Xiang, Stable and efficient $CsPbI_3$ quantum-dot light-emitting diodes with strong quantum confinement, *Nat. Commun.*, 2024, **15**, 5696.

45 X. Y. Mei, K. G. He, R. S. Zhuang, M. B. Yu, Y. Hua and X. L. Zhang, Stabilizing dynamic surface of highly luminescent perovskite quantum dots for light-emitting diodes, *Chem. Eng. J.*, 2023, **453**, 139909.

46 A. Stelmakh, M. Aebli, A. Baumketner and M. Kovalenko, On the mechanism of alkylammonium ligands binding to the surface of $CsPbBr_3$ nanocrystals, *Chem. Mater.*, 2021, **33**, 5962–5973.

47 C. H. Bi, Z. W. Yao, X. J. Sun, X. C. Wei, J. X. Wang and J. J. Tian, Perovskite quantum dots with ultralow trap density by acid etching-driven ligand exchange for high luminance and stable pure-blue light-emitting diodes, *Adv. Mater.*, 2021, **33**, 2006722.

48 S. Y. Guo, H. Liu, H. Y. He, W. Wang, L. Jiang, X. H. Xiong and L. Wang, Eco-friendly strategy to improve durability and stability of zwitterionic capping ligand colloidal $CsPbBr_3$ nanocrystals, *Langmuir*, 2020, **36**, 6775–6781.

49 M. Kim, B. G. Kim, J. Y. Kim, W. Jang and D. H. Wang, Enhanced colloidal stability of perovskite quantum dots via split-ligand re-precipitation for efficient bi-functional interlayer in photovoltaic application, *J. Ind. Eng. Chem.*, 2020, **88**, 137–147.

50 C. Würth, M. Grabolle, J. Pauli, M. Spieles and U. Resch-Genger, Relative and absolute determination of fluorescence quantum yields of transparent samples, *Nat. Protoc.*, 2013, **8**, 1535–1550.

51 R. F. Kubin and A. N. Fletcher, Fluorescence quantum yields of some rhodamine dyes, *J. Lumin.*, 1982, **27**, 455–462.

52 J. Y. Kim, B. G. Kim, W. Jang and D. H. Wang, Mesoporous trap of molecular sieves via water-selective capture for stable perovskite quantum dots, *ACS Sustainable Chem. Eng.*, 2022, **10**, 1115–1124.

53 J. R. Martins, V. Krivenkov, C. R. Bernardo, P. Samokhvalov, I. Nabiev, Y. P. Rakovich and

M. I. Vasilevskiy, Statistical analysis of photoluminescence decay kinetics in quantum dot ensembles: Effects of inorganic shell composition and environment, *J. Phys. Chem. C*, 2022, **126**, 20480–20490.

54 W. Z. Lv, L. Li, M. C. Xu, J. X. Hong, X. X. Tang, L. G. Xu, Y. H. Wu, R. Zhu, R. F. Chen and W. Huang, Improving the stability of metal halide perovskite quantum dots by encapsulation, *Adv. Mater.*, 2019, **31**, 1900682.

55 A. Rudawska and E. Jacniacka, Analysis for determining surface free energy uncertainty by the Owen-Wendt method, *Int. J. Adhes. Adhes.*, 2009, **29**, 451–457.

56 C. Liu, J. Tu, X. T. Hu, Z. Q. Huang, X. C. Meng, J. Yang, X. P. Duan, L. C. Tan, Z. Li and Y. W. Chen, Enhanced hole transportation for inverted tin-based perovskite solar cells with high performance and stability, *Adv. Funct. Mater.*, 2019, **29**, 1808059.

57 D. W. Huang, P. F. Xie, Z. X. Pan, H. S. Rao and X. H. Zhong, One-step solution deposition of $CsPbBr_3$ based on precursor engineering for efficient all-inorganic perovskite solar cells, *J. Mater. Chem. A*, 2019, **7**, 22420–22428.

58 Y. S. Shin, K. Lee, Y. R. Kim, H. Lee, I. M. Lee, W. T. Kang, B. H. Lee, K. Kim, J. Heo, S. Park, Y. H. Lee and W. J. Yu, Mobility engineering in vertical field effect transistors based on van der Waals heterostructures, *Adv. Mater.*, 2018, **30**, 1704435.